

Multi-mode fiber reservoir computing overcomes shallow neural networks classifiers

Daniele Ancora^{1,3,*}, Matteo Negri¹, Antonio Gianfrate², Dimitris Trypogeorgos²,

Lorenzo Dominici², Daniele Sanvitto², Federico Ricci-Tersenghi^{1,3,4}, and Luca Leuzzi³

¹*Department of Physics, Università di Roma la Sapienza, Piazzale Aldo Moro 5, I-00185 Rome, Italy*

²*Institute of Nanotechnology, Consiglio Nazionale delle Ricerche (CNR-NANOTEC), Via Monteroni, I-73100 Lecce, Italy*

³*Institute of Nanotechnology, Soft and Living Matter Laboratory,*

Consiglio Nazionale delle Ricerche (CNR-NANOTEC), Piazzale Aldo Moro 5, I-00185 Rome, Italy and

⁴*Istituto Nazionale di Fisica Nucleare, sezione di Roma1, Piazzale Aldo Moro 5, I-00185 Rome, Italy*

(Dated: October 11, 2022)

In disordered photonics, one typically tries to characterize the optically opaque material in order to be able to deliver light or perform imaging through it. Among others, multi-mode optical fibers are extensively studied because they are cheap and easy-to-handle complex devices. Here, instead, we use the reservoir computing paradigm to turn these optical tools into random projectors capable of introducing a sufficient amount of interaction to perform non-linear classification. We show that training a single logistic regression layer on the data projected by the fiber improves the accuracy with respect to learning it on the raw images. Surprisingly, the classification accuracy performed with physical measurements is higher than the one obtained using the standard transmission matrix model, a widely accepted tool to describe light transmission through disordered devices. Consistently with the current theory of deep neural networks, we also reveal that the classifier lives in a flatter region of the loss landscape when trained on fiber data. These facts suggest that multi-mode fibers exhibit robust generalization properties, thus making them promising tools for optically-aided machine learning.

Keywords: Multi-mode fibers, reservoir computing, disordered photonics, neural networks, classification, MNIST.

I. INTRODUCTION

A sound understanding of the huge success of Neural Networks (NNs) in learning processes and inference tasks is still lacking. A fundamental point is to understand why such architectures, that can have even billions of parameters, do not severely overfit data, as predicted by statistical learning theory and the so-called *bias-variance trade-off* (see for example [1] or [2]). The abundance of learnable parameters, in fact, is arguably the most universal feature in the zoo of NN architectures. Interestingly, it is known that, once the NN architecture is set, most of the model parameters adapts little-to-nothing during the learning procedure [3, 4], suggesting the idea that random projections may play an equally important role in NNs. Recent works, in fact, have shown that it is possible to train a simple two-layer model by learning only the upper layer, interpreting the first one as a random projection [5, 6]. These results were further strengthened by Baldassi et al. [7], who proved that increasing the dimension of the random projection leads to the production of special states in the loss landscape (the function that is minimized during the training of the model), which are related to the good generalization properties in neural networks. Finally, recent evidence is provided [8] that the way the random projection is chosen is fundamental to determine the generalization properties of the upper layer of these simple models. This suggests that differ-

ent classes of random (possibly non-linear) projections impact differently on the performance of the models.

In this context, the class of optical neural networks (ONN), else termed photonic neuromorphic computing [9] in a broader sense, is a promising field of research that provides high-speed, high-throughput computing architectures. One of the advantages of using optical hardware is, in fact, that neurons can be made interacting by exploiting light scattering [10–12] and photon interference [13, 14]. Unfortunately, for a fine tuning of the ONN optical parameters, an accurate modeling of the whole optical system is required to perform consistent back-propagation update [15]. This is often difficult to accomplish due to the so called *reality gap* that becomes relevant when the model does not perfectly describe the physical system. In many cases, a missing detail in the modeling of the overall physical mechanisms at work in the real system lowers the performance of the whole architecture [16, 17], requiring some additional software-level corrections [11]. To mitigate these effects, hybrid strategies were proposed to enforce the training [15], as well as using deep learning to aid the modeling of the physical system [17].

In place of modeling complex physical systems, some approaches directly *make use* of the non-linear outputs determined by the physics of the hardware itself. The underlined computation scheme is called *reservoir computing* (RC) [18] and relies on the fact that the hardware is doing some unknown but pre-determined computation, yielding a highly non-linear response. Typically one exploits RCs to perform a given task (i.e., classification [19]), training a single software layer feeding the output

* daniele.ancora@uniroma1.it

response of the reservoir as an input dataset. Among these RC systems, the wider the neuron connectivity, the better the gain in performance. The reservoir approach is robust against a possible reality gap since it does not require knowledge of what the hardware is exactly doing. At the moment, however, the choice of the reservoir is restricted to a collection of delicate physical systems (such as polaritons [19], disordered dopant-atom network [20], dynamic memristors [21]) that require low temperature, sensitive alignment, and expensive hardware. These considerations motivated our interest in exploiting the RC stability to produce a non-linear output response for classification using the most straightforward optical configuration available.

For these reasons, the class of random projections realized by an optical multi-mode fiber (MMF) appears to be an ideal candidate for RC. The modes entering the MMF are, in fact, mixed together in a way that is conceptually similar to what an ideal reservoir does. These devices scramble the light due to numerous scattering events, effectively creating a random interference image — the so called speckle pattern — on the output side. Although the transmission of light can be regarded as a linear process, interference effects take place when dealing with the measurement of the light-field intensity. Because of this, we decided to exploit MMFs to carry out classification tasks as an RC unit, which provides random projections depending on its state. We do this by comparing MMF performances to those obtained with random Gaussian linear projections and to that of a transmission matrix approach, which is the model that is commonly used to describes light propagation in disordered structures [22, 23]. By doing this, we pursue two objectives: making a proof of concept for a hardware-based neural network using optical fibers, and studying the characteristic of complex-valued random projections that we found to be essential for good performance, with the aim of deepening the understanding of neural networks. In fact, we will see that standard linear modeling of the hardware turns out to be a source of a substantial reality gap even for a MMF, making the advantage of reservoir computing not needing a model even more relevant.

Our idea stems from the common assumption that a generic multi-mode fiber transports light by a linear process [22]. In this regime, light propagation can be described by a simple multiplication of the input signal by a matrix that contains the transmission rule as:

$$\mathbf{y} = \mathbb{T}\mathbf{x}. \quad (1)$$

In this descriptive model, \mathbf{x} is the controlled input, \mathbb{T} is the (complex-valued and typically unknown) transmission matrix of the medium, and \mathbf{y} is the output field. Despite this, the way we measure the output is not linear at all, mainly for two reasons. First, photons carry complex signals, i.e., the electromagnetic field associated to each propagation mode is characterized by amplitude and phase. Current electronic devices cannot follow the rapid field oscillation and this renders impossible to di-

rectly measure the phase information. Considering an eventual readout additive noise ε , the camera only sees the intensity distribution:

$$|\mathbf{y}|^2 = |\mathbb{T}\mathbf{x}|^2 + \varepsilon. \quad (2)$$

Second, the camera has a well defined sensitivity range that depends on each pixels capability to store intensity change. If the signal reaching a given pixel exceeds the sensitivity, the measure turns to be clipped at the peak (overexposure) and/or at the bottom (underexposure). This effect can be seen as a saturation of the input signal for both high and low intensities and is hardly a linear phenomenon. These considerations imply that the readout of a coherent field is non-linear. In analogy to machine learning terminology, this can be described by a strongly non-linear *activation function* $\sigma(\cdot)$, applied on the result of a complex-valued linear transmission.

By admitting underexposure only, for instance, the camera activation process can be represented by using the rectified linear unit function (ReLU):

$$\sigma(\mathbb{T}\mathbf{x}) = \max\left(0, |\mathbb{T}\mathbf{x}|^2 + \varepsilon - b\right), \quad (3)$$

where the quantity b describes the intensity threshold under which the measure is not recorded.

The problem of retrieving the whole, complex, transmission from intensity measurements, thus, is non-linear as is extensively documented in literature [22–28]. Having as its main goal the exploitation of the MMF as an optical tool for image recovery or focus delivery, many approaches aimed at solving this riddle rather than exploiting its random projection properties, beginning with the four-phases method [22], down to Bayesian optimization [29], or iterative Gerchberg-Saxton schemes [30, 31]. It is not the scope of this paper, however, to characterize the device and circumvent the limitations of the measuring process. Instead, we want to exploit the multi-modal random nature of the fiber to perform reservoir computing: we interpret the fiber as an optical analogous of a pre-trained neural network composed by a single “hidden layer”. In this shallow architecture, the MMF layer already contains a particular realization of static weights (the reservoir), that depends upon the physical status of the optical fiber. This property allows to perform random but deterministic projections at the speed of light with a fixed transmission matrix, which are, then, read out by the camera. In particular, if we enter with only a few modes in the input facet of an MMF that supports many more, the output will still be completely triggered, implying a mapping of the kind few-to-many. If that is the case, our optical hidden layer (i.e., MMF *and* camera) is capable of performing fully-connected random projections on a higher dimensional space. At this stage, we have all the ingredients to perform non-linear optical computation [32] also with inexpensive and large, thus easier to handle in a setup, optical multi-mode fibers. The goal of this study is to carry out image classification by concatenating a software-trained linear layer to the measured

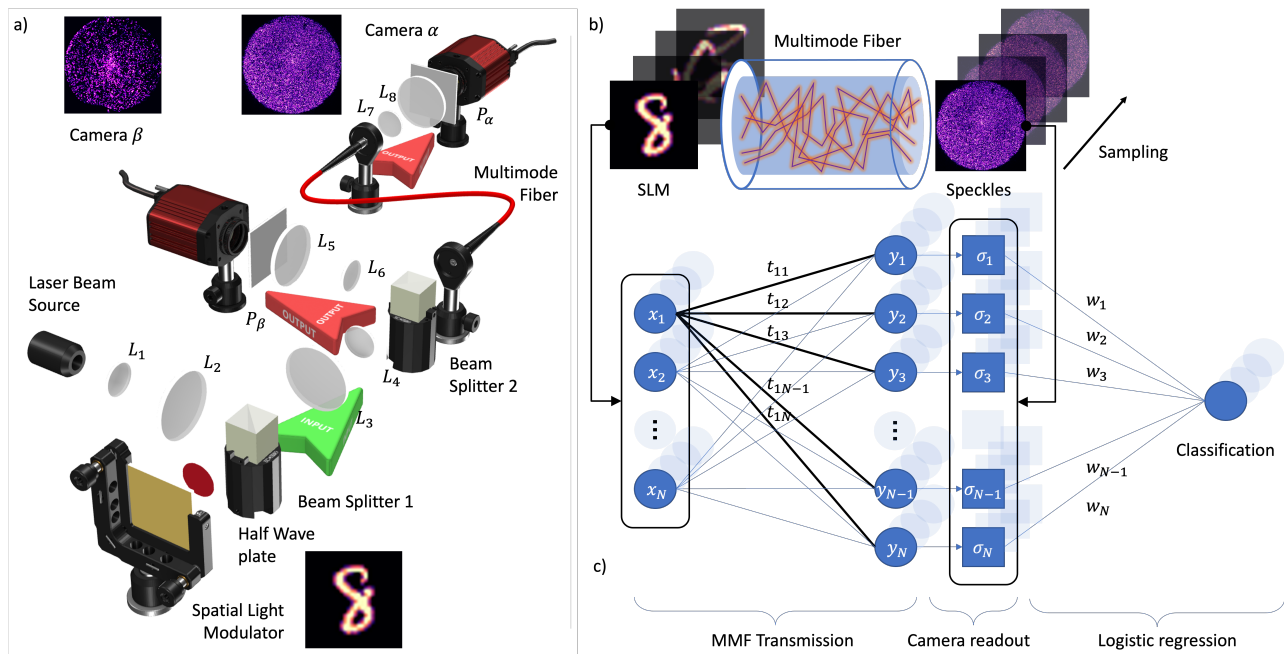


FIG. 1. Schematics of the shallow optical neural network with the MMF. Panel a), simplified scheme of light transport through multi-mode fibers. The MNIST data set, modulated by a spatial light modulator, enters the MMF on the input facet. During propagation, the light gets scrambled with a random but deterministic process, giving rise to the speckle pattern measured in the camera. Panel b), corresponding neural network interpretation of the light propagation scheme. The MNIST set constitutes the input vector of a linear complex layer with static weights. The non-linear operation is determined by the camera that reads the intensity of a complex field. Successively, a linear classification layer is trained using the output of the fiber. Panel c), scheme of the imaging setup.

output of a MMF, produced by inserting a given image from the dataset into the input edge of the fiber.

II. RESULTS AND DISCUSSIONS

We choose to approach the MNIST classification problem in order to carry out a widely studied non-linear task. The only parameters that we train are those of a simple logistic regression layer, which is known to achieve poor performances on the standard MNIST set, reaching a maximum classification accuracy of 92.7% [19]. Exploiting random projection provided by the MMF, an optical device that is known to be linear, we compare with the performances obtained using reference datasets. In this study, we train the parameters of the logistic classifier using six different input datasets:

1. Original MNIST. It is formed by $l \times l$ images, with $l = 28$, at the original resolution of the standard MNIST set. We use the accuracy performance of this set as the baseline of our study.
2. Randomized MNIST. We shuffle the original MNIST set linearly by multiplying it with a Gaussian random matrix with positive entries. This maps the dataset into a higher dimension space, producing images with a side $L \gg l$ pixels.

3. Upscaled MNIST. Each image, with original resolution ($l \times l$), is expanded by a factor L/l using a linear spline interpolation achieving the target size of $L \times L$.
4. MMF α -cam. The speckled output of the MMF is recorded with a resolution of $L \times L$. Each speckle pattern is produced by sending the MNIST images (of size $l \times l$) on the input edge of the fiber, recording the output after disordered propagation.
5. MMF β -cam. Same as the previous one, with the speckles being recorded on the same input facet as that of the light injection. A relatively small portion of the light propagating forward is internally reflected and comes back towards the input edge. This determines a different speckle realization that we acquire as an independent measurement.
6. Simulated MMF. The MMF is characterized retrieving its underlined transmission matrix \mathbb{T} via the SmoothGS protocol [31]. Then, we used the inferred transmission matrix in order to simulate the propagation of the $l \times l$ MNIST set with Eq. (1), recording the simulated speckle pattern by storing only the squared modulus.

All the datasets were used for a supervised training, in which the image of the MNIST set is associated to the

number that represents, and the speckle image is associated to the classified number corresponding to the MNIST image impinged onto the fiber. Further details of the training procedure can be found in the Appendix section 1. To exclude possible dependence on the problem size, we choose to set the size of the randomized and up-scaled MNIST sets to have the same dimension as the recorded fiber output. This implies that the same number of parameters are trained while solving the classification problem for every dataset, the only exception being the original set. In the following, we report the average results obtained by running independent logistic regressions on each dataset, comparing the classification accuracy on a test set composed by 1000 numbers isolated from the original set.

In experiment 1, we used 10^4 MNIST images, randomly picking up to 9000 images for training and 1000 images for testing. We repeat the parameter optimization for a total of $T = 100$ times, varying the number of training samples to test the robustness of our results and analyze statistics. From Fig. 2a, we see how the performances of the MNIST dataset (original, randomized, and upscaled) are similar one to another. The classification problem, in fact, is well known to be a non-linear task, and hardly generalizes using a linear model alone. Instead, using the MMF reservoir higher performances are achieved, approaching 96% test accuracy on average on the largest set used (9000 train examples).

We stress that this accuracy is not high in absolute terms since deep neural networks with convolutional layers have been able to reach more than 99% test accuracy on MNIST [33], with modern deep architectures raising even up to 99.91% [34]. As we will discuss in more detail in section III, the strength of our approach lies in its simplicity. Compared to those, the model architecture consists only of a linear classifier after a purely hardware random projector layer. With this straightforward setup, the MMF permits to substantially improve the results obtained against a plain linear classifier (88% accuracy with 9000 train examples).

We also underline that we did not use the full MNIST dataset (which is composed of 60000 images for training and 10000 for testing) but a fraction of it; by increasing the number of training samples, the trend in Fig. 2 seems to suggest that there is room for improvement. Already after ~ 500 samplings, the gain provided by our approach starts to become evident, and with only 9000 images, we can achieve performance that can hit $\sim 97\%$. We point out that to achieve the highest accuracy with the experimental data (stars and crosses in the plot of Fig. 2a), we tested several independently initialized optimizations. Interestingly, this turns out to be independent of the microscopic MMF arrangement, as the two different transmission rules underlined by the α and β detections perform almost identically.

As a final note on experiment 1, we recall that we did not fine-tune the hyperparameters of the classifier, so we can expect that their meticulous choice (mainly the l_2 -

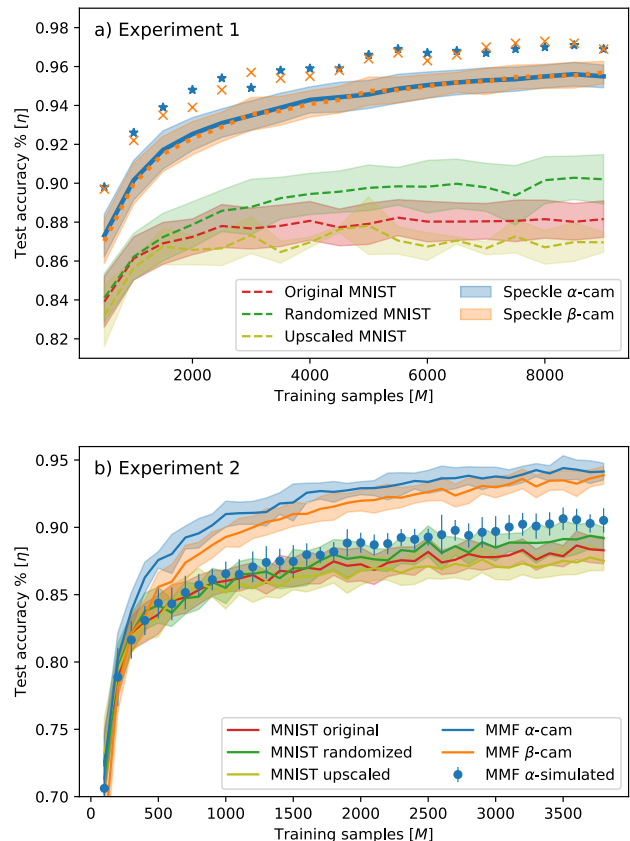


FIG. 2. Logistic regression performance using different training datasets. a) in the experiment 1, we perform the training with up to nine thousand images. The original MNIST set (resolution 28×28) was used as reference performance (red line) for the logistic regression, together with its upscaled (light green) and randomized (green) versions. Training the classifier with the speckled images (blue and orange) obtained by using the MMF to transform the MNIST exhibited the highest accuracy. We sampled several independent trainings, and we reported with the asterisk plot the best performance obtained with the fiber. b) in experiment 2, we train using up to 3800 images. Compared to the plot in panel a), here we include also the output of the simulated fiber. The simulation was done by recovering the transmission matrix of the optical element, and using a complex linear transmission model. Surprisingly, the simulated model performs better than the MNIST set but did not reach the same performance as its experimental counterpart.

regularization strength and the stopping threshold) could improve the accuracy curves for all the datasets. However, we are not interested in the absolute numbers: our scope is to highlight the improvement determined by the physics of interactions of the MMFs, whereas a performance shift provided by the fine tuning of the hyperparameters with respect to each dataset would not change the take home message.

The results obtained in experiment 1 are consistent with those of experiment 2. In experiment 2, we take

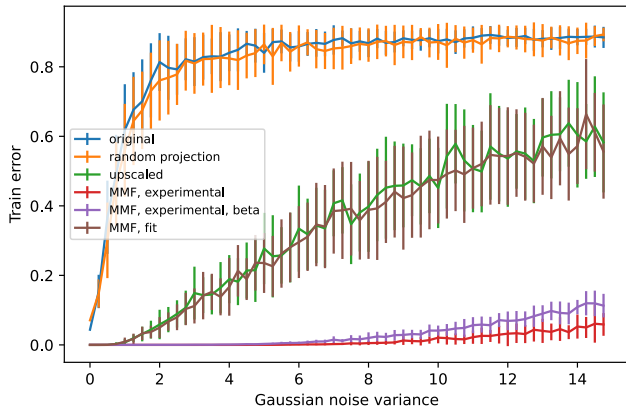


FIG. 3. Local energy profiles for models trained on the different projected datasets. Each point corresponds to the train error of configurations sampled with multiplicative noise around the reference, averaged over 30 samples. The reference configurations are models trained on 3800 examples. Error bars show the standard deviation of the error distribution.

a different static configuration of the fiber in which we alternatively probe the fiber with random and MNIST images. The output given by random images was used with the sole scope of estimating the transmission of the fiber using the SmoothGS protocol [31]. After having recovered the transmission matrix \mathbb{T} , we use it to simulate the MNIST dataset after fiber propagation that obey to Eq. 2. Interestingly, using the retrieved \mathbb{T} to simulate the optical transmission through the MMF fiber does not perform as the experimental data. It does slightly better than the direct MNIST set, but far from being comparable with the performance obtained with the recorded speckles (Fig. 2b). This reality gap may be due to the presence of noise and other non-linearities that appear experimentally and are not represented in the way we model the physics of the system of Eq. 3 at low power. It might be conjectured that high power non-linearities, also studied in the framework of computational optics with much more intense pulsed light [32] already contributes at the lower intensities we have been using in our experiments. We leave the investigation of the causes of this gap to further studies. The data acquired by the β -cam was intentionally strongly underexposed with respect to the α -dataset (see the App. 4). By doing so, we notice that substantial thresholding determines a marginally negative impact on the method performance, especially if compared with a better filling of the camera dynamic range in Fig. 2b. On the other hand, we also observe that, even when the camera loses most of the signal, the accuracy of the classifier drops only by a factor of $\sim 2\%$. The weak performance drop appears surprising and possibly supports the idea that the MMF provides random transformations that are particularly robust to carry out classification tasks.

Discussion on random projections Our study can be seen as a testing ground for different random projectors

used to pre-train the MNIST dataset, looking for those that ease the classification task. In order to understand why the best accuracy results are obtained with MMFs, we study a measure of the flatness of the energy landscape (train error) around the different model solutions. Flatness is supposed to correlate well with generalization properties [7, 35–39] and can provide insights into how the geometry of the projected space influences the hardness of the classification problem. We use the method of the *local energy* to measure the flatness (see [7] and references therein), that consists in adding a multiplicative Gaussian noise to the model parameters, sampling configurations with a given noise, and eventually computing the average classification error (see Appendix section 2 for all the details). Performing this procedure for increasing noise values yields an estimate of the flatness of the reference configuration. In Fig. 3, we see that the local energy profile correlates well with test accuracy shown in Fig. 2: the flattest the solutions, the better the test accuracy (with the exception of the upscaled dataset). A remarkable feature of the local energy profiles of MMF solutions is that they appear stable up to the noise of the order of 10 times the signal-to-noise ratio. This robustness to noise might be the reason for the excellent generalization performance.

MMFs, then, appear as promising candidates for reservoir computing. The models trained on MMF-projected data show very low local energy variation. On one hand, this confirms the current idea in the literature that flatness correlates with generalization; on the other hand, it raises the question of why MMFs exhibit such a conceptual difference with their idealized model. In fact, the linear transmission model performs worse than the real MMFs when we study classification accuracy as a reservoir. This reality gap could signal something not yet taken into account in the theoretical description of the physics of experimental set-ups with MMFs.

III. PERSPECTIVES

In this work, we used MMFs to realize random transformations of the MNIST dataset showing that a linear classifier has better accuracy on the MMF-transformed dataset than on the original one. Complementary to high-intensity pulsed excitation [32], this transformation (MMF and camera detection) is non-linear even in continuous low-power regime and increases the dimension of the data, but those characteristics are not enough to justify improved accuracy alone. In fact, we did not manage to achieve performances similar to the transformation provided by MMF by comparing data upscaling (that increases the dimension), random matrix multiplication (that projects on random space), and a model that simulates the MMF behavior (that performs a non-linear operation). As anticipated in section II, our goal is not to compete with the accuracy of more complicated architectures but rather to show that an MMF is a simple

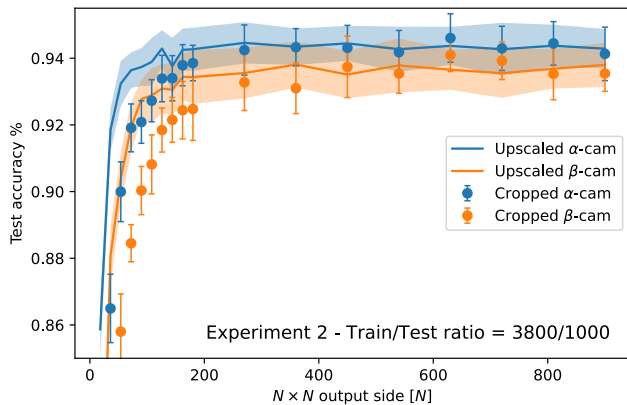


FIG. 4. Training accuracy trade-off when reducing the number of output fiber modes in experiment 2. With solid lines, we study the performances obtained using de-magnified camera outputs as a function of their output size. With dots, we report the same study cropping a central window within the speckled image recorded by the camera. For both, we notice that performances remain stable down to a substantial reduction of the number of modes used in the training set (around 400 pixels, 80% less pixel than the full resolution dataset).

—yet robust— candidate for reservoir computing. For example, convolutional neural networks exploit spatial correlations in the data and work particularly well for image datasets. Our approach is, instead, closer to that of a fully connected network, leaving room for applicability to different variety of data types. However, contrarily to general random transformations (that destroy spatial correlations), the fiber output presents a correlation property determined by the average size of the speckle patterns. We do not exclude exploiting this feature with a convolutional approach, similarly to the SmoothGS introduced in [31].

An MMF used as a reservoir is cheap, can flexibly be mounted to deliver light in a user-defined position, and offers a different set of random projections each time it is positioned (thus needing independent training of the output layer). Indeed, we still need an expensive SLM and at least one camera to record the speckled projection, but those are almost unavoidable in any ONNs configuration. In general, the MMF approach can be compared to other attempts to use hardware to improve software classification models. To the best of our knowledge, the current state-of-the-art is achieved using FPGA hardware in conjunction with data augmentation, reaching 98% test accuracy [40]. Another approach using disordered optical media exploits polaritons to reach 96% accuracy [41], which is comparable with average optimizations obtained with the MMF approach. These considerations strengthen the fact that MMFs are promising tools for hardware reservoir computing, with the additional advantage of their simplicity and easiness of use. Our results are also relevant for the theoretical understanding of deep neural networks: in the spirit of random-feature

models [5–7], we showed that the class in which we sample the random features plays important role in the accuracy, as suggested in [8]. In fact, while taking a Gaussian random matrix already improves the accuracy a bit, the transformation implemented by an MMF makes a much bigger difference.

Further investigation is needed to understand why the specific hardware transformation provided by the MMF is so effective. Here, we put forward some conjectures based on the present study. First, the fact that the accuracy gap between the physical MMF data and its simulation (Fig. 2) is reflected in the local energy profile (Fig. 3) makes us confident that the two approaches indeed belong to different classes of random transformations. The fact the physical MMF transformation is so robust to perturbations is consistent with the great redundancy of the data that emerges from Fig. 4 and Fig. 5, where we see that we can delete the majority of the signal before losing accuracy. We conjecture that the random transformation realized by MMFs leads to well-separated projections in the high-dimensional space that allow for a good classification accuracy that is also resistant to noise, in a way that is reminiscent of error-correcting codes.

ACKNOWLEDGMENTS

We thank Dr. Raffaele Marino for useful discussions. We acknowledge the support from the European Research Council (ERC) under the European Union’s Horizon 2020 Research and Innovation Program, Project LoTGLasSy (Grant Agreement No. 694925, Prof. Giorgio Parisi). We also acknowledge the support of LazioInnova - Regione Lazio under the program *Gruppi di ricerca 2020* - POR FESR Lazio 2014-2020, Project NanoProbe (Application code A0375-2020-36761).

1. Neural network architecture and training procedure

Our classification model involves a fully connected layer that maps linearly the 28×28 image space into a higher dimensional $N = 900 \times 900$ output space. On the output space, we build a linear classification model using the *LogisticRegression* function provided by the python library RapidsAi [42], the GPU equivalent of the Scikit-Learn implementation. Given an input pattern $\{\xi_i\}_{i=1,\dots,N}$ the *LogisticRegression* function performs a weighted average of the N input channels, producing a score $z_j = \sum_{i=1}^N w_{ji}\xi_i$ for each of the 10 classes corresponding to each type of digit. The scores are then transformed to probabilities with

$$p_j = \frac{e^{z_j}}{\sum_{j'=1}^{10} e^{z_{j'}}} \quad (4)$$

and plugged in a cross-entropy loss function that is a sum of contributions coming from all of the P input patterns

that we are using to train the model

$$L(\mathbf{w}) = - \sum_{\mu=1}^P \log(p_{j^*}) \quad (5)$$

where j^* is the index of the correct class of each input pattern. The cross-entropy loss $L(\mathbf{w})$ is then minimized with a gradient-descent-related strategy to find the configuration of the weights \mathbf{w}^* that has the highest classification accuracy.

2. Measure of local energy

Given a loss (namely energy) function L that depends on a set of parameters \mathbf{w} , we define the local energy as the following expectation value

$$L_{\text{local}}(\sigma) = \mathbb{E}_{\eta_{ij} \sim \mathcal{N}(0, \sigma)} L(\{w_{ij} \eta_{ij}\}) \quad (6)$$

where $\{\eta_{ij}\}$ is a set of i.i.d. random Gaussian variables with zero mean and variance σ that multiply element-wise the set model parameters $\{w_{ij}\}$. The local energy $L_{\text{local}}(\sigma)$ still depends on the variance σ of the Gaussian noise. As explained in the main text, we are interested in studying how quickly the local energy increases when we increase σ : from the literature (see main text) we know that a slower increase is correlated with a higher test accuracy.

3. Experimental setup

The sketch of the experimental setup is shown in Fig. 1c. In the experiment, we used a Melles Griot he-ne laser is the laser source (632.8nm) as laser source. The emitted beam is magnified 15 times through a 5 : 75cm telescope before being imprinted on a Hamamatsu SLM in polarization configuration (model LCOS-SLM x10488 series, pixel size: 20 μm). The real space plane of the SLM is then recreated on the entrance facet of the optical fiber using a pair of 50 : 7.5cm focal lenses after the spatially modulated beam profile has been collected. Thorlabs FT-1.0-EMT, $NA = 0.39$, 1 meter long, 1mm core multi-mode optical fiber is the one that has been utilized. We indicate each facet of the MMF with the letter α and β . Two IDS cameras (UI-5370CP-M-GL and UI-5480CP-M-GL) with pixel sizes of 5.5 and 2.2 μm , respectively, are used to collect the counter-polarized (respect to the laser) reflection from the injection surface as well as the transmission signal. To achieve the same spatial resolution of 1.1 $\mu\text{m}/px$ on both cameras, the magnification was set to 5 \times and 3 \times respectively. The MNIST handwritten digits and random masks are alternated in the SLM patterns, which are encoded in 11-degree gray scale using 28 \times 28 blocks. The random patterns are sent for the sole purpose of the characterization of the fiber transmission, and are not used for training of the classification layer. The light propagating through this disordered optical device reaches both edges and produces a

seemingly random interference pattern of intensities (the speckles).

4. Under-exposure, camera saturation, and measurement stability

When setting the exposure time of the camera, we are implicitly acting on the way it records the signal. If the exposure time is fast enough with respect to the intensity delivered, the camera underexposes the signal, i.e. does not detect the signal in a particular region. The opposite effect, over-exposure, happens when intensity is too high compared to a long exposure of the images. In both cases, a non-linear threshold is introduced in the detected signals. To try to assess its effect on the classifier accuracy, we tried to explore several intensity distributions of the datasets recorded in camera. In experiment 1, Fig. 5a, α -cam provides an optimal dynamic range, with low under- (0.1%) and over-exposure (1%). Instead, the β -cam recorded the signal underexposing 7% of the total pixels in the image. In experiment 2, Fig. 5b, the α -cam correctly sample the intensities, whereas β -cam is set to cut off 37% of the pixels. Additionally, we report also the intensity distribution obtained with the simulation of the light propagating through the fiber and detected by the α -cam. We notice a substantial difference between the intensity distribution of the recorded and simulated data: this could explain the different performances achieved by the two datasets.

Over the entire duration of the experiment, we continuously monitored the fiber stability by sending to the SLM an identical image. When the fiber is sufficiently stable, the speckle pattern produced at the facets must be always identical to the ones recorded at the beginning of the experiment. Keeping the camera frame $\tau = 0$ as a reference for both α, β cameras, we computed the normalized scalar product against the speckle image at a given time τ' :

$$\rho(\tau, \tau') = \frac{s_{\tau}^{\{\alpha, \beta\}} \cdot s_{\tau'}^{\{\alpha, \beta\}}}{\left| s_{\tau}^{\{\alpha, \beta\}} \right|^2}, \quad (7)$$

where we called s the speckle pattern recorded at the time. Using this metric, $\rho \approx 1$ means the measurements are highly correlated whereas $\rho \approx 0$ implies that the system decorrelated during the measurement. Fig. 6 reports the stability study across the entire duration of the experiment 1. We notice that the α -cam remains highly correlated (96% minimum), compared to the β -cam (90% minimum). Despite the lower correlation stability and 7% underexposed pixels values, the β -cam resulted as accurate as the α cam during the classification of the test set (Fig.2).

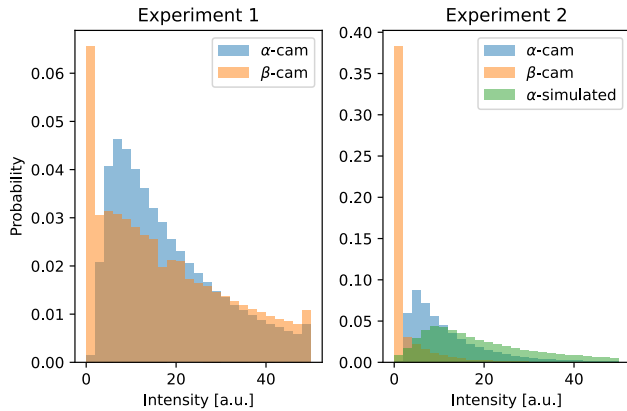


FIG. 5. Intensity distribution of the speckle pattern measured in camera α and β during two independent experiments. Given a stable laser output, we modify the camera exposure time to force a certain amount of non-linearity (in the form of a recording threshold) in the measuring process. a) In experiment 1, the dynamic range of the camera α fits well the intensity distribution of the speckle images recorded, whereas camera β underexposes around 7% of the signal. b) In experiment 2, the camera α have a similar trend to that of experiment 1, but in camera β we strongly underexpose the images, cutting out 37% of the light intensity reaching the sensor.

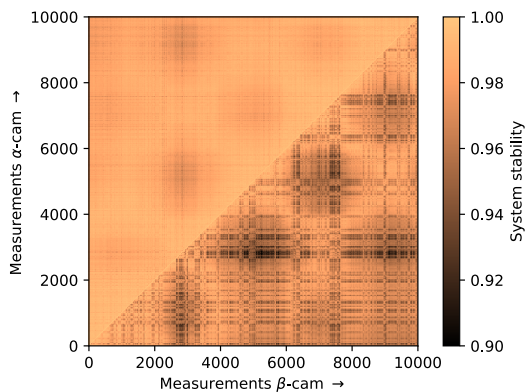


FIG. 6. Measurement stability during experiment 1. Keeping the initial probing frame, we compute the normalized scalar product against the output of the same frame at different time for both α, β cams. The upper half of the plot is the correlation stability of the α -cam (thus how similar the output look when the same input is sent again during the experiment) and the bottom one for β . In both cases the correlation remained higher than 90%.

-
- [1] T. Hastie, R. Tibshirani, and M. Wainwright, *Statistical Learning with Sparsity, The Lasso and Generalizations* (CRC Press, Taylor & Francis Group, 2003).
 [2] D. J. MacKay, *Information theory, inference and learning*

- algorithms* (Cambridge university press, 2003).
 [3] L. Chizat, E. Oyallon, and F. Bach, *Advances in Neural Information Processing Systems* **32** (2019).
 [4] M. Geiger, S. Spigler, A. Jacot, and M. Wyart, *Journal*

- of Statistical Mechanics: Theory and Experiment **2020**, 113301 (2020).
- [5] F. Gerace, B. Loureiro, F. Krzakala, M. Mézard, and L. Zdeborová, in *International Conference on Machine Learning* (PMLR, 2020) pp. 3452–3462.
- [6] S. Goldt, B. Loureiro, G. Reeves, F. Krzakala, M. Mézard, and L. Zdeborová, in *Mathematical and Scientific Machine Learning* (PMLR, 2022) pp. 426–471.
- [7] C. Baldassi, C. Lauditi, E. M. Malatesta, R. Pacelli, G. Perugini, and R. Zecchina, *Phys. Rev. E* **106**, 014116 (2022).
- [8] G. Perugini, (private communication).
- [9] L. De Marinis, M. Cococcioni, P. Castoldi, and N. Andrioli, *IEEE Access* **7**, 175827 (2019).
- [10] X. Lin, Y. Rivenson, N. T. Yardimci, M. Veli, Y. Luo, M. Jarrahi, and A. Ozcan, *Science* **361**, 1004 (2018).
- [11] T. Zhou, X. Lin, J. Wu, Y. Chen, H. Xie, Y. Li, J. Fan, H. Wu, L. Fang, and Q. Dai, *Nature Photonics* **15**, 367 (2021).
- [12] J. Li, D. Mengu, N. T. Yardimci, Y. Luo, X. Li, M. Veli, Y. Rivenson, M. Jarrahi, and A. Ozcan, *Science Advances* **7**, eabd7690 (2021).
- [13] Y. S. Abu-Mostafa and D. Psaltis, *Scientific American* **256**, 88 (1987).
- [14] Y. Shen, N. C. Harris, S. Skirlo, M. Prabhu, T. Baehr-Jones, M. Hochberg, X. Sun, S. Zhao, H. Larochelle, D. Englund, *et al.*, *Nature photonics* **11**, 441 (2017).
- [15] J. Spall, X. Guo, and A. I. Lvovsky, *Optica* **9**, 803 (2022).
- [16] Y. Zuo, B. Li, Y. Zhao, Y. Jiang, Y.-C. Chen, P. Chen, G.-B. Jo, J. Liu, and S. Du, *Optica* **6**, 1132 (2019).
- [17] L. G. Wright, T. Onodera, M. M. Stein, T. Wang, D. T. Schachter, Z. Hu, and P. L. McMahon, *Nature* **601**, 549 (2022).
- [18] G. Tanaka, T. Yamane, J. B. Héroux, R. Nakane, N. Kanazawa, S. Takeda, H. Numata, D. Nakano, and A. Hirose, *Neural Networks* **115**, 100 (2019).
- [19] D. Ballardini, A. Gianfrate, R. Panico, A. Opala, S. Ghosh, L. Dominici, V. Ardizzone, M. De Giorgi, G. Lerario, G. Gigli, *et al.*, *Nano Letters* **20**, 3506 (2020).
- [20] T. Chen, J. van Gelder, B. van de Ven, S. V. Amitonov, B. De Wilde, H.-C. Ruiz Euler, H. Broersma, P. A. Bobbert, F. A. Zwanenburg, and W. G. van der Wiel, *Nature* **577**, 341 (2020).
- [21] C. Du, F. Cai, M. A. Zidan, W. Ma, S. H. Lee, and W. D. Lu, *Nature communications* **8**, 1 (2017).
- [22] S. M. Popoff, G. Lerosey, R. Carminati, M. Fink, A. C. Boccara, and S. Gigan, *Physical review letters* **104**, 100601 (2010).
- [23] D. Ancora and L. Leuzzi, *Journal of Physics A: Mathematical and Theoretical* **55** (2022).
- [24] E. G. van Putten and A. P. Mosk, *Physics* **3**, 22 (2010).
- [25] S. Popoff, G. Lerosey, M. Fink, and et al., *Nat Commun* **1**, 81 (2010).
- [26] J. Aulbach, B. Gjonaj, P. M. Johnson, A. P. Mosk, and A. Lagendijk, *Phys. Rev. Lett.* **106**, 103901 (2011).
- [27] S. M. Popoff, A. Goetschy, S. F. Liew, A. D. Stone, and H. Cao, *Phys. Rev. Lett.* **112**, 133903 (2014).
- [28] S. Rotter and S. Gigan, *Rev. Mod. Phys.* **89**, 015005 (2017).
- [29] A. Drémeau, A. Liutkus, D. Martina, O. Katz, C. Schülke, F. Krzakala, S. Gigan, and L. Daudet, *Optics express* **23**, 11898 (2015).
- [30] G. Huang, D. Wu, J. Luo, L. Lu, F. Li, Y. Shen, and Z. Li, *Photonics Research* **9**, 34 (2021).
- [31] D. Ancora, L. Dominici, A. Gianfrate, P. Cazzato, M. De Giorgi, D. Ballardini, D. Sanvitto, and L. Leuzzi, arXiv preprint arXiv:2112.09564 (2022).
- [32] U. Teğın, M. Yıldırım, İ. Oğuz, C. Moser, and D. Psaltis, *Nature Computational Science* **1**, 542 (2021).
- [33] Y. Lecun, L. Bottou, Y. Bengio, and P. Haffner, *Proceedings of the IEEE* **86**, 2278 (1998).
- [34] S. An, M. Lee, S. Park, H. Yang, and J. So, arXiv preprint arXiv:2008.10400 (2020).
- [35] Y. Jiang, B. Neyshabur, H. Mobahi, D. Krishnan, and S. Bengio, “Fantastic generalization measures and where to find them,” (2019), arXiv:1912.02178 [cs.LG].
- [36] C. Baldassi, A. Ingrosso, C. Lucibello, L. Saglietti, and R. Zecchina, *Phys. Rev. Lett.* **115**, 128101 (2015).
- [37] C. Baldassi, C. Borgs, J. T. Chayes, A. Ingrosso, C. Lucibello, L. Saglietti, and R. Zecchina, *Proceedings of the National Academy of Sciences* **113**, E7655 (2016), <https://www.pnas.org/content/113/48/E7655.full.pdf>.
- [38] P. Chaudhari, A. Choromanska, S. Soatto, Y. LeCun, C. Baldassi, C. Borgs, J. Chayes, L. Sagun, and R. Zecchina, *Journal of Statistical Mechanics: Theory and Experiment* **2019**, 124018 (2019).
- [39] F. Pittorino, C. Lucibello, C. Feinauer, E. M. Malatesta, G. Perugini, C. Baldassi, M. Negri, E. Demyanenko, and R. Zecchina, arXiv preprint arXiv:2006.07897 **2021**, 124015 (2020).
- [40] A. Morán, C. F. Frasser, M. Roca, and J. L. Rosselló, *IEEE Transactions on Computers* **69**, 392 (2020).
- [41] R. Mirek, A. Opala, P. Comaron, M. Furman, M. Król, K. Tyszka, B. Seredynski, D. Ballardini, D. Sanvitto, T. C. Liew, *et al.*, *Nano letters* **21**, 3715 (2021).
- [42] R. D. Team, *RAPIDS: Collection of Libraries for End to End GPU Data Science* (2018).